



Cite this: DOI: 10.1039/d1ta01729b

Structure-induced partial phase transformation endows hollow TiO₂/TiN heterostructure fibers stacked with nanosheet arrays with extraordinary sodium storage performance†

Pan Xue,^{‡a} Qiulong Li,^{‡ad} Wenbin Gong,^{‡c} Zhongti Sun,^b Han Wang,^a Kaiping Zhu,^a Can Guo,^a Guo Hong,^{‡*fg} Weigao Xu,^h Jingyu Sun,^{‡b} Yagang Yao^{‡*a} and Zhongfan Liu^{‡be}

The construction of a heterointerface by structure-induced partial phase transformation is an effective strategy to synchronously boost conductivity and regulate the ion diffusion kinetics of TiO₂ considered as an anode material for sodium ion batteries. However, construction of a highly conductive heterostructure in well-crystallized TiO₂ is still a great challenge. Herein, a structure-induced partial phase transformation method is reported to synthesize hierarchical hollow TiO₂/TiN heterostructure fibers (HTTFs) with a high specific surface area for use as an anode. The interfacial effect of the heterostructures for the anode materials could improve charge transfer capability. The improvement of the conductivity is due to the electric field generated inside the nanocrystals, which greatly reduces the ion diffusion resistance of nanocrystals and promotes the interfacial electron transport. Density functional theory calculations and experimental results demonstrate that HTTFs greatly facilitated the mobility of holes and ion diffusion, which result in excellent rate capability (270.9 and 113.1 mA h g⁻¹ at 50 and 10 000 mA g⁻¹, respectively) and excellent cycling stability (132.5 mA h g⁻¹ with an average capacity fading of only 0.002% per cycle at 5000 mA g⁻¹ over 10 000 cycles). Such improvements signify that suitable heterogeneous interface design provides an innovative and versatile approach for achieving advanced battery materials.

Received 27th February 2021
Accepted 21st April 2021

DOI: 10.1039/d1ta01729b

rsc.li/materials-a

Introduction

Sodium ion batteries (SIBs) are promising alternatives to lithium ion batteries (LIBs) as next generation energy storage

systems because of their low cost and similar intercalation mechanism associated with high natural reserve abundance of sodium resources.^{1–5} However, it is difficult to find suitable materials to effectively and sustainably regulate sodium ion embedding/de-embedding, because the sodium ion (1.02 Å) is much larger than the lithium ion (0.76 Å).^{6,7} Titanium dioxide (TiO₂) has been usually considered as a promising candidate anode owing to its abundant resources, high theoretical capacity (335 mA h g⁻¹), and low volume expansion upon desodiation/sodiation.^{8–11} Nevertheless, the poor intrinsic conductivity generated by the large band gap (3.0 eV) and the sluggish ion diffusion kinetics of pure crystal TiO₂ seriously limits its practical applications.^{12,13}

In order to solve these problems, some previously reported results have certified that the construction of heterojunctions can significantly improve the intrinsic electronic conductivity of electrode materials.^{14–19} However, high-crystallized TiO₂ is not conducive to the introduction of other heterogeneous substances and deep doping. Surface amorphization is an important strategy to achieve deep doping of heteroatoms. But it requires harsh experimental conditions and is not conducive to large-scale preparation. Furthermore, low concentration doping will only introduce local oxygen vacancy states, which

^aNational Laboratory of Solid State Microstructures, College of Engineering and Applied Sciences, Nanjing University, Nanjing 210093, China. E-mail: ygao2018@nju.edu.cn

^bCollege of Energy, Soochow Institute for Energy and Materials Innovations (SIEMIS), Key Laboratory of Advanced Carbon Materials and Wearable Energy, Technologies of Jiangsu Province, Soochow University, Suzhou 215006, China

^cSchool of Physics and Energy, Xuzhou University of Technology, Xuzhou 221018, China

^dCollege of Materials Science and Engineering, Nanjing Tech University, 30 Puzhu Road, Nanjing 211816, China

^eCenter for Nanochemistry (CNC), College of Chemistry and Molecular Engineering, Peking University, Beijing 100871, China

^fInstitute of Applied Physics and Materials Engineering, University of Macau, Avenida da Universidade, Taipa, Macau SAR 999078, China. E-mail: ghong@um.edu.mo

^gDepartment of Physics and Chemistry, Faculty of Science and Technology, University of Macau, Avenida da Universidade, Taipa, Macau SAR 999078, China

^hKey Laboratory of Mesoscopic Chemistry, School of Chemistry and Chemical Engineering, Nanjing University, Nanjing 210093, China

† Electronic supplementary information (ESI) available. See DOI: 10.1039/d1ta01729b

‡ These authors contributed equally.

will destroy electron mobility.^{20–22} Thereby, when the doping is adequately deep, it can significantly decrease the band gap range of TiO₂ and further increase its conductivity.^{23–26} Generally, semiconductors or impurity atoms with poor conductivity are mostly used in the construction of heterogeneous interfaces (N,^{27–29} B,³⁰ P²⁰ or S^{21,31}); it will limit partial charge transfer during charging/discharging processes. Consequently, it is necessary to obtain highly conductive and homogeneously deep doping materials, which can be acquired by surface amorphization with a simple method.

In recent years, TiN has attracted more and more attention due to its high electrical conductivity and stable physicochemical properties, but its large volume expansion during charging and discharging processes is not beneficial for further applications.^{17,32–36}

Therefore, it is extremely challenging to realize uniform doping of TiN and construct the field effect of the heterogeneous interface in block TiO₂. Herein, a simple structure-induced partial phase transition strategy was proposed for the purpose of improving the electrical conductivity and sodium ion diffusion ability of anode materials by the interfacial effect. Multi-stage hollow TiO₂/TiN heterostructure fibers (HTTFs) were obtained by adjusting the ammonia treatment time. Compared with the heterostructure synthesized by traditional methods, the hollow structure of HTTFs is beneficial to the diffusion of ammonia gas for deep TiN doping and electrolyte infiltration. It is noted that the uniform distribution of highly conductive TiN in HTTFs increases the conductivity of electrode materials, and the heterogeneous interface formed with TiO₂ generates an ideal interface effect to promote ion/electron diffusion during the cycling process. This was confirmed by density functional theory (DFT) calculations. Meanwhile, the multistage array structure can increase the specific surface area as well as the number active sites and reduce the sodium ion transfer paths for enhancing the SIB rate performance. Furthermore, the hollow structure of HTTFs can alleviate the effect of volume expansion and nanoclusters.

Profiting from these advantages, HTTFs electrodes exhibited relatively high reversible capacity (270.9 mA h g⁻¹, 50 mA g⁻¹), high-rate performance (113.1 mA h g⁻¹ at an ultrahigh current density of 10 000 mA g⁻¹), and remarkable cycling capacity (132.5 mA h g⁻¹ after 10 000 cycles at 5000 mA g⁻¹). This work provides an effective strategy to improve the storage kinetics of sodium ions through the introduction of multistage arrays and heterogeneous structures. The heterostructure operation strategy constructed by *in situ* structural induction of partial phase transition can also be extended to other transition metal oxide electrodes for energy storage and conversion.

Results and discussion

The HTTFs formed by stacking array-like nanosheets can promote the transfer of ions and electrons (Fig. 1a). Density functional theory (DFT) calculations were performed in this study to investigate the performances of the HTTFs. The TiO₂(101) surface and HTTFs composite interface model was constructed in Fig. S1.† The calculated density of states (DOS)

clearly shows that HTTFs possess excellent electrical conductivity, which comes from not only the metallic TiN but also the n-type doped TiO₂ (the Fermi level locates around the CBM of TiO₂) as illustrated in Fig. 1c, while the pure TiO₂ is well known as a wide gap semiconductor (Fig. 1b). From the charge density difference of HTTFs as shown in Fig. 1d, the n-type doping of TiO₂ could also be confirmed. It is found that electrons are depleted from the TiN (cyan isosurfaces) and accumulated on the TiO₂ (isosurfaces). Here, we introduced the plane-averaged electron density differences to visualize electron redistribution, which suggests negative charge accumulation on the TiO₂ side and positive one on the TiN side, respectively. This leads to a built-in electric field to accelerate the Na ion diffusion at the interface of HTTFs. Compared with the diffusion barrier of Na ions in the bulk TiO₂ (0.56 eV), the barrier dramatically reduced by 70% to only 0.16 eV as shown in Fig. 1e and f. As a result, it is convincing that the combination of TiO₂ and TiN has the ability of pronouncedly enhancing the performances of the battery.

Firstly, TiO₂ fiber precursors were successfully obtained through electrostatic spinning technology, and then TiO₂ precursors formed multistage array hollow TiO₂ nanofibers after low-temperature annealing and heat treatment with alkali water solvent. The heterostructure of TiO₂/TiN with different content ratios was formed by controlling the ammonia treatment time, as shown in Fig. 2a. *In situ* doping of TiN can significantly reduce the aggregation and increase the conductivity of TiO₂. The HTTFs as negative materials for sodium ion batteries demonstrate higher capacity and excellent rate performance, in comparison with pure TiO₂.

The morphology of the sample after heat treatment with solvent was characterized by scanning electron microscopy (SEM). The pristine TiO₂ consists of a lot of array “flakes” stacked together and the average diameter of the hollow fiber is about 750 nm (Fig. S2a–d)†. After ammonia treatment, the fiber size is basically unchanged and the size of flakes on the fiber surface slightly decreases (Fig. 2b and c). To further observe the hollow structure of the HTTFs, transmission electron microscopy (TEM) was conducted as depicted in Fig. 2d. It can be clearly seen that the HTTFs indeed exhibit a hollow structure and their surface is porous.

In order to demonstrate the phase change of the pure TiO₂ surface, high-resolution TEM (HRTEM) and selected-area electron diffraction (SAED) were employed to characterize the samples. As shown in Fig. S3c,† the lattice fringes with spacings of 0.35 and 0.23 nm were measured for the pure TiO₂, which correspond to the (101) and (200) crystal planes of TiO₂, respectively. Fig. S3d,† presents the SAED pattern of the TiO₂, indicating its single crystalline nature. After ammonia treatment, the crystalline (101) planes of TiO₂ (lattice spacing of 0.35 nm) can still be observed, while a new spacing of 0.21 nm, corresponding to the (200) planes of TiN (Fig. 2e) was also observed.^{32,37} The SAED pattern of the TiO₂/TiN shown in Fig. 2f reveals the polycrystalline nature of the TiO₂/TiN. Furthermore, scanning transmission electron microscopy (STEM) energy dispersive spectroscopy (EDS) mapping of the HTTFs was employed, certifying an uniform distribution of N, O, and Ti elements in the HTTFs (Fig. 2g).

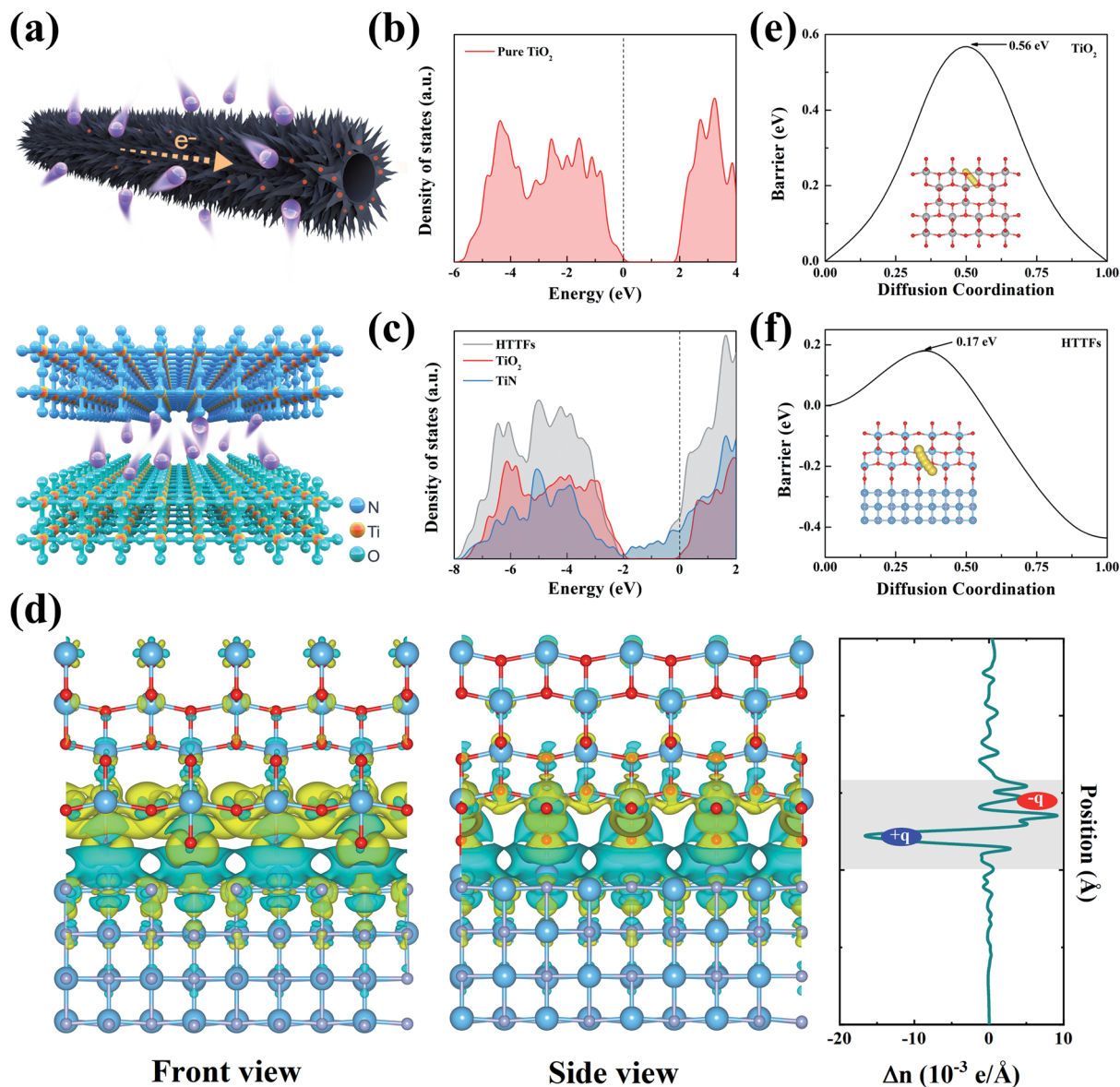


Fig. 1 (a) Schematic of the path for sodium ion diffusion/electron conduction in HTTFs and the structural model of the heterogeneous interface of HTTFs. Calculated density of states (DOS) of pure TiO₂ (b) and projected DOS of HTTFs (c). (d) Charge density difference of HTTFs from the front view and side view, as well as the plane-averaged electron density differences as a function of Z-position. The yellow and cyan isosurfaces present charge accumulation and depletion, respectively. Calculated diffusion barriers of the Na ion in bulk TiO₂ (e) and the interface of HTTFs (f).

The crystal phases of HTTFs and pure TiO₂ at various ammonia treatment times were characterized by X-ray diffraction (XRD), as exhibited in Fig. 3a. All of the samples exhibited the duplicate phase structure of anatase TiO₂ (JCPDS #78-2486). The major diffraction peaks at $2\theta = 25.30^\circ, 37.79^\circ, 48.07^\circ, 53.88^\circ, 55.07^\circ, 62.69^\circ, 68.76^\circ, 70.29^\circ,$ and 75.05° belong to the (101), (004), (200), (105), (211), (204), (116), (220), and (215) planes of anatase TiO₂. However, after 0.5–2 h ammonia treatment, some new diffraction peaks were observed at $2\theta = 33.54^\circ$ and 43.25° , which belong to the (111) and (200) planes of TiN and no other diffraction peaks were detected, indicating that TiO₂ and TiN co-existed in the synthesized HTTFs-0.5, 1, and 2 h (Table S1†). In addition, compared with the pristine TiO₂, with

the increase of ammonia treatment time, the diffraction peak intensity of TiO₂ gradually decreased and that of TiN gradually increased, demonstrating that the nitrogen degree for the HTTFs gradually increases. This can be attributed to the hollow array structure of the HTTFs, which facilitates ammonia diffusion and deep doping.²⁵

X-ray photoelectron spectroscopy (XPS) characterization was used to investigate the surface chemical states and the elemental compositions of TiO₂ before and after the ammonia treatment, as shown in Fig. 3b–d and S4.† From the survey spectra in Fig. S4a and d,† the peaks of N were observed for TiO₂/TiN, proving the successful production of TiN. And the high-resolution XPS spectra of Ti 2p, N 1s and O 1s are displayed

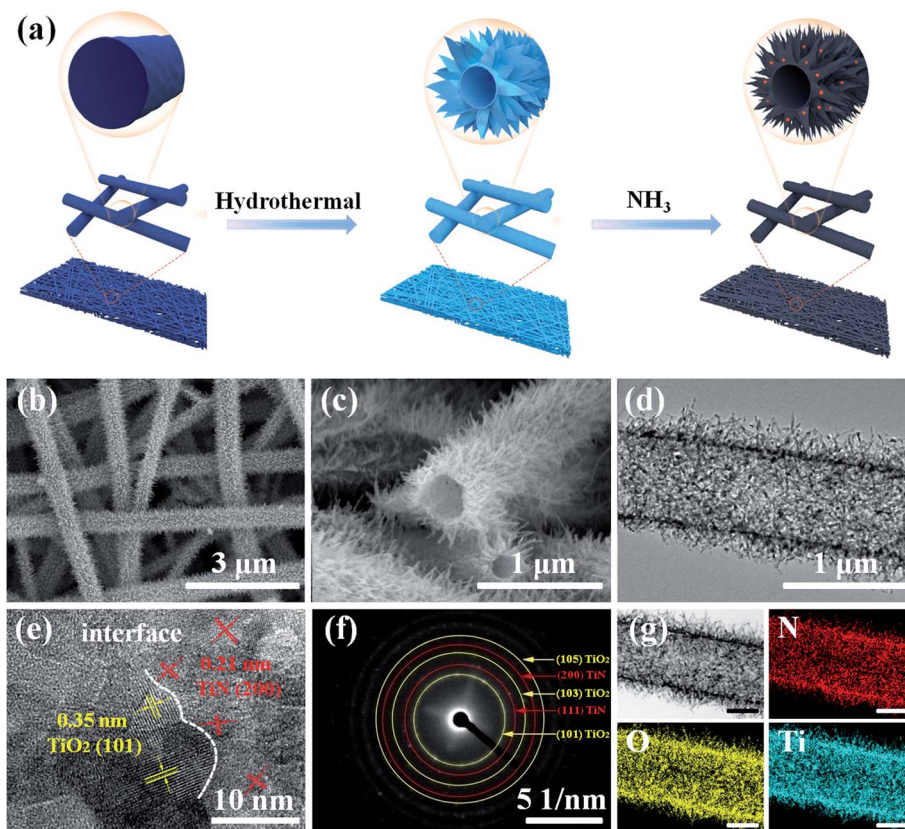


Fig. 2 (a) Schematic of the synthesis process for HTTFs. (b) Top-view SEM images of the top surface of the HTTFs. (c) Cross-sectional SEM images showing HTTFs hosts with a fiber diameter of 750 nm. (d) TEM, (e) HRTEM and (f) selected-area electron diffraction images of the HTTFs. (g) Element map of HTTFs.

in Fig. 3b–d. For the HTTFs-1h sample, the three peaks located at 455.4, 456.85 and 461.3 eV can be assigned to the Ti–N and Ti–N–O, which can be ascribed to the replacement of O sites by N (Fig. 3b). As shown in the N 1s XPS spectra, HTTFs-1h displayed three peaks located at 395.93, 397.4 and 399.3 eV, assigned to the Ti–N, Ti–N–O bonds and absorbed-N, respectively (Fig. 3c),^{32,33,38–41} further demonstrating the generation of TiN. Meanwhile, the O 1s spectrum of HTTFs-1h contains two peaks at 529.80 and 531.30 eV, corresponding to the Ti⁴⁺–O bond and Ti³⁺–O bond (Fig. 3d). What's more, compared with the pure TiO₂ sample, the Ti 2p and O 1s spectra of the HTTFs-1h sample show a slight shifting toward a high binding energy in Fig. S5,† further indicating the formation of oxygen vacancies. And the fitting results reveal that the ratio of lattice oxygen to oxygen vacancies according to the peak area for the HTTFs-1h sample is higher than that of the pure TiO₂ sample, suggesting that more oxygen vacancies are introduced during ammonia treatment.³⁸

Nitrogen Brunauer–Emmett–Teller (BET) adsorption was performed to characterize the specific surface area and pore-size distribution of pure TiO₂, HTTFs-0.5h, HTTFs-1h, HTTFs-2h and Pure TiN samples (Fig. 3e and f). As the ammonia treatment time increases, the specific surface area of the samples generally increases first and then decreases (Table S2†). The increased specific surface area of the composite

samples was mainly due to the formation of more hetero-junction interfaces and lattice defects by the increase of the ammonia treatment time. However, when TiO₂ is completely converted to TiN, the more reaction time is conducive to obtaining materials with higher crystallinity. Furthermore, after hydrothermal treatment, the size of branched TiO₂ increased owing to its exposure, further boosting the diffusion of ammonia and the uniform doping of TiN. The large number of uniform TiO₂/TiN heterogeneous interfaces significantly improved the sodium storage performance of anatase TiO₂.

In order to prove the superiority of the interfacial effect produced by the structurally induced partial TiO₂ conversion into highly conductive TiN for the sodium storage of TiO₂, the electrochemical performances of the samples were investigated. The first charge and discharge curves of all samples at 200 mA g^{−1} in Fig. 4a exhibit a similar tendency within the voltage range of 0.01 to 3.0 V, with an obvious platform between 1.0 and 1.25 V, which can be attributed to the solid electrolyte interphase (SEI) membrane and electrolyte side reactions during the first discharge.²⁰ Such results are also confirmed by the cyclic voltammetry (CV) curves in Fig. 4b. The two irreversible peaks in the first cycle were due to the formation of the SEI membrane and the irreversible decomposition of the electrolyte.^{21,42–45} During the following cycles, the wide cathodic/anodic peaks at approximately 0.68/0.86 V corresponded to the

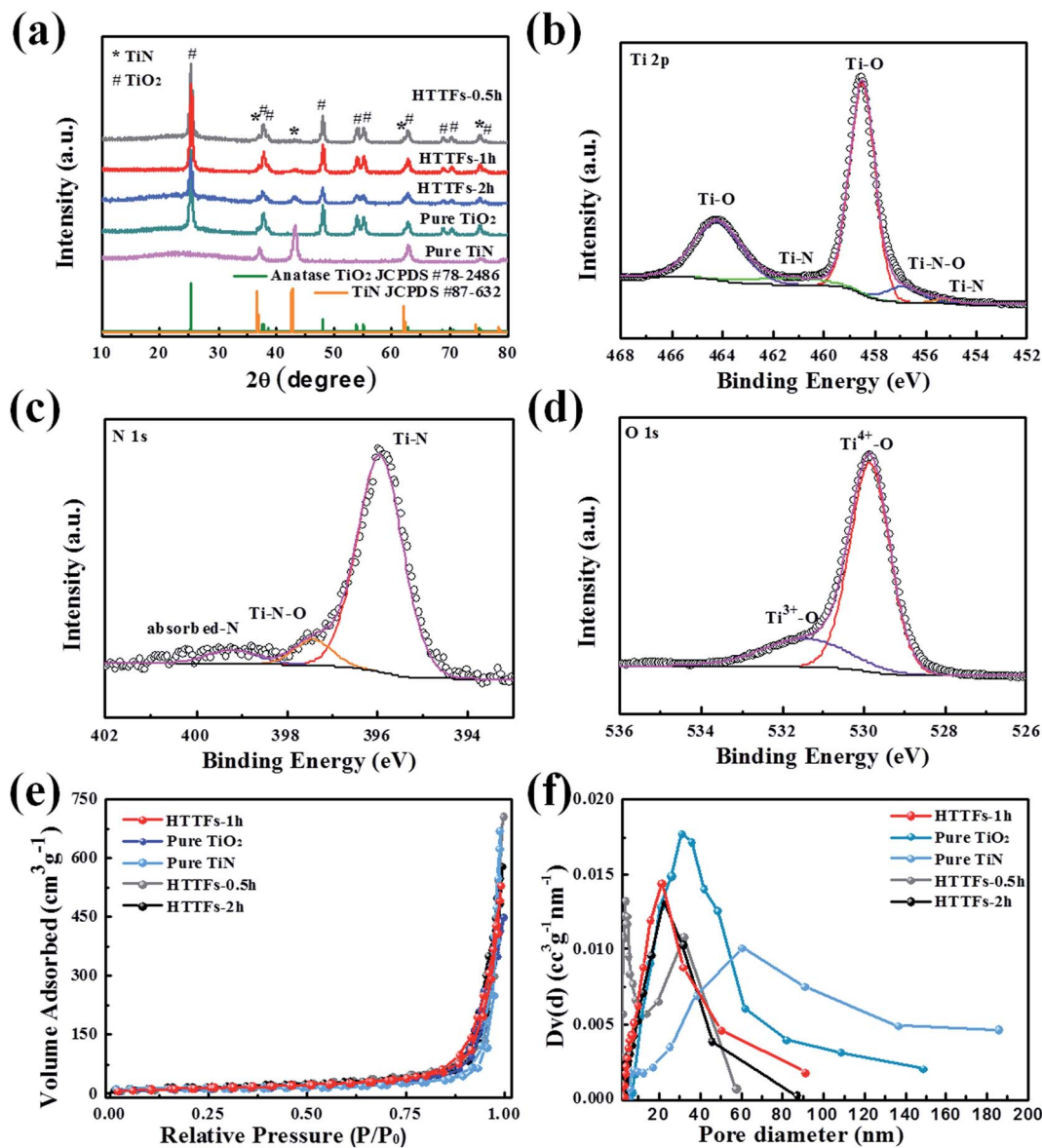


Fig. 3 (a) XRD patterns of the HTTFs-0.5h, HTTFs-1h, HTTFs-2h, pure TiO_2 and TiN samples. XPS characterization of HTTFs-1h; (b–d) core-level spectra of Ti 2p, N 1s and O 1s peaks. (e and f) Pore size distribution curves and nitrogen adsorption–desorption isotherms of HTTFs-1h, HTTFs-0.5h, HTTFs-2h, pure TiO_2 and TiN.

reversible $\text{Ti}^{3+}/\text{Ti}^{4+}$ oxidation and reduction reactions accompanied by Na ion insertion and deinsertion.^{21,38} Additionally, a small peak appears at 0.1 V, which is ascribed to the reaction between acetylene black and sodium ions. Obviously, HTTFs-1h exhibits excellent cycling stability and higher discharge capacity (Fig. 4c), and the discharge capacity was $188.7 \text{ mA h g}^{-1}$ after 200 cycles at a current density of 200 mA g^{-1} , which is much higher than that of pure TiO_2 ($126.3 \text{ mA h g}^{-1}$), pure TiN ($104.1 \text{ mA h g}^{-1}$), HTTFs-2h ($168.4 \text{ mA h g}^{-1}$) and HTTFs-0.5h ($160.3 \text{ mA h g}^{-1}$) (Fig. S6†). As expected, the ammonia treatment time for the samples plays a significant key for the electrochemical performances. This is mainly because appropriate TiN doping can establish a good heterogeneous interface. Under ammonia treatment for 0.5 h, the doping concentration

of TiN is not enough to effectively form an interface effect that can accelerate charge transfer. When the ammonia treatment time reaches 2h, the TiN content in the system increases, but TiN has large volume expansion during charging and discharging, leading to a poor cycle performance for Na ion batteries. Therefore, the doping concentration and the intrinsic conductivity of TiN have a positive effect on improving the sodium storage performance of TiO_2 .

The excellent sodium storage performance of the TiO_2/TiN heterostructure after ammonia treatment for 1 h is further emphasized by its superior rate capability, as shown in Fig. 4d. HTTFs-1h exhibits discharge capacities of 270.9, 222.3, 194.9, 163.2, 150.2, and $139.6 \text{ mA h g}^{-1}$ at 50, 100, 200, 500, 1000, and 2000 mA g^{-1} , respectively. Even at ultrahigh current densities of

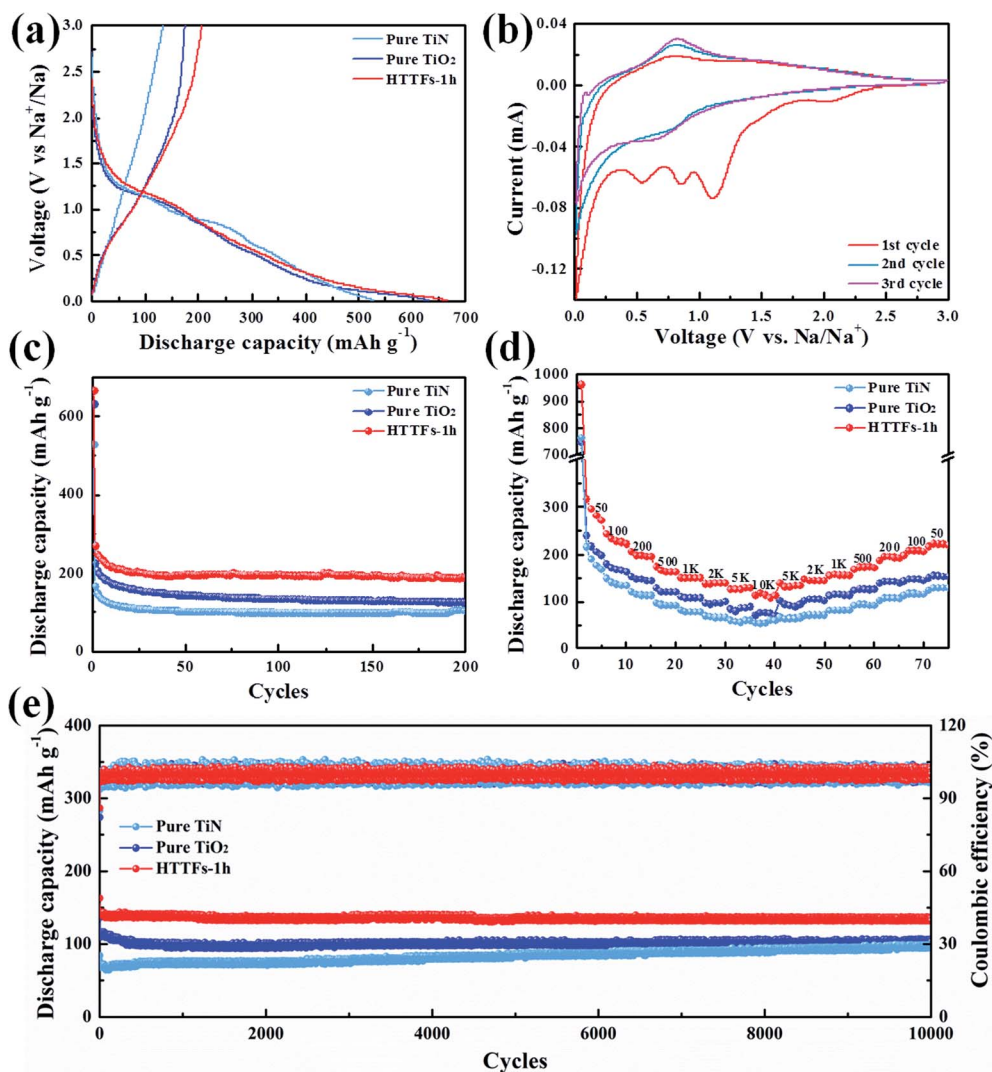


Fig. 4 (a) Charge/discharge profiles of HTTFs-1h, pure TiO₂ and TiN at 200 mA g⁻¹ (b) cyclic voltammogram of HTTFs-1h with a scan rate of 0.1 mV s⁻¹. (c) Cycling performance of HTTFs-1h, pure TiO₂ and TiN at 200 mA g⁻¹ for 200 cycles. (d) Rate performance of HTTFs-1h, pure TiO₂ and TiN at different current densities. (e) Cycling performance of HTTFs-1h, pure TiO₂ and TiN at 5000 mA g⁻¹ for 10 000 cycles.

5000 mA g⁻¹ and 10 000 mA g⁻¹, the discharge capacities still remain at 129.5 and 113.1 mA h g⁻¹, respectively, exhibiting an outstanding rate performance of HTTFs-1h. It is worth noting that when the current density returned to 50 mA g⁻¹ and 218.9 mA h g⁻¹ discharge capacity is obtained, indicating excellent reversibility. Particularly, the discharge capacity of HTTFs-1h is almost twice that of pure TiO₂ (69.9 mA h g⁻¹) and TiN (60.2 mA h g⁻¹) at a current density of 10 000 mA g⁻¹. Furthermore, HTTFs-0.5h and HTTFs-2h deliver discharge capacities of 93.2 mA h g⁻¹ and 101.4 mA h g⁻¹ at a current density of 10 000 mA g⁻¹, respectively, which are also much higher than those of pure TiO₂ and TiN. These remarkable results are attributed to the increase in the diffusion kinetics of sodium ions caused by the interfacial effect and the doping of highly conductive TiN. Moreover, the unobstructed sodium ion diffusion channel constructed by the arrayed nanosheets significantly improved the rate performance of HTTFs. And the hollow fiber structure design is more favorable for the complete

infiltration of the electrolyte and fast charge transfer.⁴⁶ In addition, the band gap of the HTTFs has been significantly reduced by introducing the heterostructures, resulting in a significant increase in the conductivity. As shown in Fig. 4e, the long-term cycle stability of HTTFs-1h, pure TiO₂ and TiN was evaluated at a high current density of 5000 mA g⁻¹. Strikingly, the discharge capacity still maintains 132.5 mA h g⁻¹ ≈ 100% Coulomb efficiency after 10 000 cycles for HTTFs-1h, proving its prominent tolerance under ultra-fast insertion/extraction of Na⁺. It is worth noting that HTTFs-1h did not show obvious lattice changes and agglomeration after 1000 cycles (Fig. S8†). Compared with previously reported TiO₂-based materials for Na ion batteries (Fig. S9 and Table S3†), the as-prepared HTTFs electrodes exhibit dramatically remarkable cycle performance, because the uniformly dispersed heterostructure significantly accelerates the charge transfer and inhibits the nano-aggregation phenomenon.

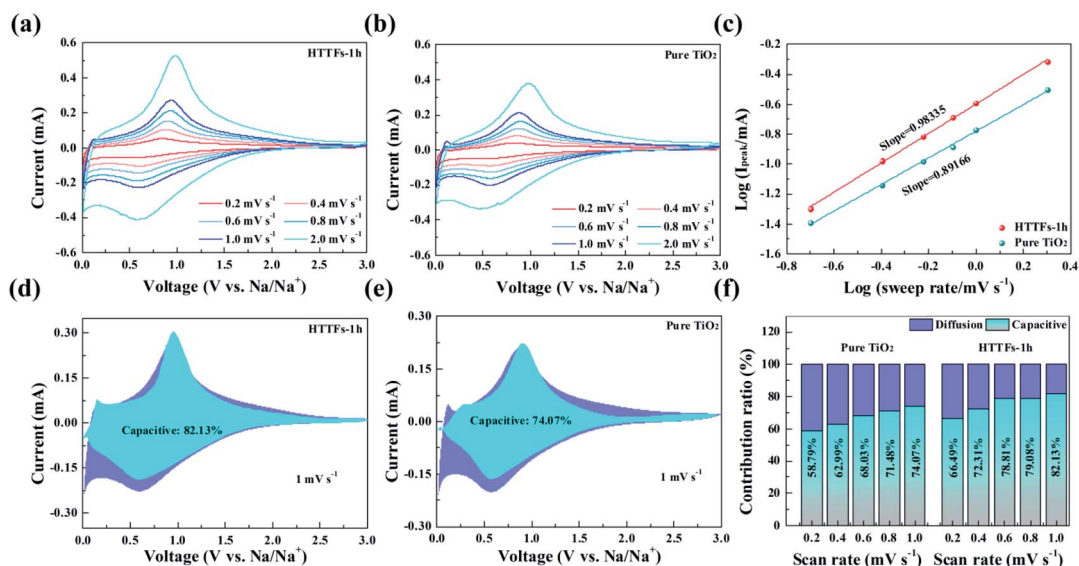


Fig. 5 (a and b) CV curves at different scan rates from 0.2–2 mV s^{-1} for HTTFs-1h and pure TiO_2 . (c) The relationship and fitted lines between $\log(v)$ and $\log(i)$. (d) and (e) Separation of the capacitive and diffusion-controlled charges of HTTFs-1h and pure TiO_2 at 1 mV s^{-1} . (f) Capacitance-controlled and diffusion-controlled contributions of the HTTFs-1h and pure TiO_2 samples.

Previously reported results proved that a self-built electric field triggered by a reasonable interface design can accelerate ion diffusion and electron transfer.^{16,17} In order to verify the influence of the interfacial effect on the diffusion of sodium ions, the electrochemical impedance spectroscopy (EIS) curves for all samples are exhibited in Fig. S10.† HTTFs show lower solid phase diffusion resistance and charge transfer resistance than a pure TiO_2 electrode (Table S4†).

In order to explain the effect of the interface effect on the storage of sodium ions, the contribution of pseudocapacitance for the HTTFs was analyzed by investigating the kinetics of electrode separation capacitance-controlled and diffusion-controlled capacity. As shown in Fig. 4a, no obvious plateau can be found on the charge and discharge curves, manifesting that the energy storage mechanism of HTTFs is mainly capacitance-controlled. To better understand the reasons for

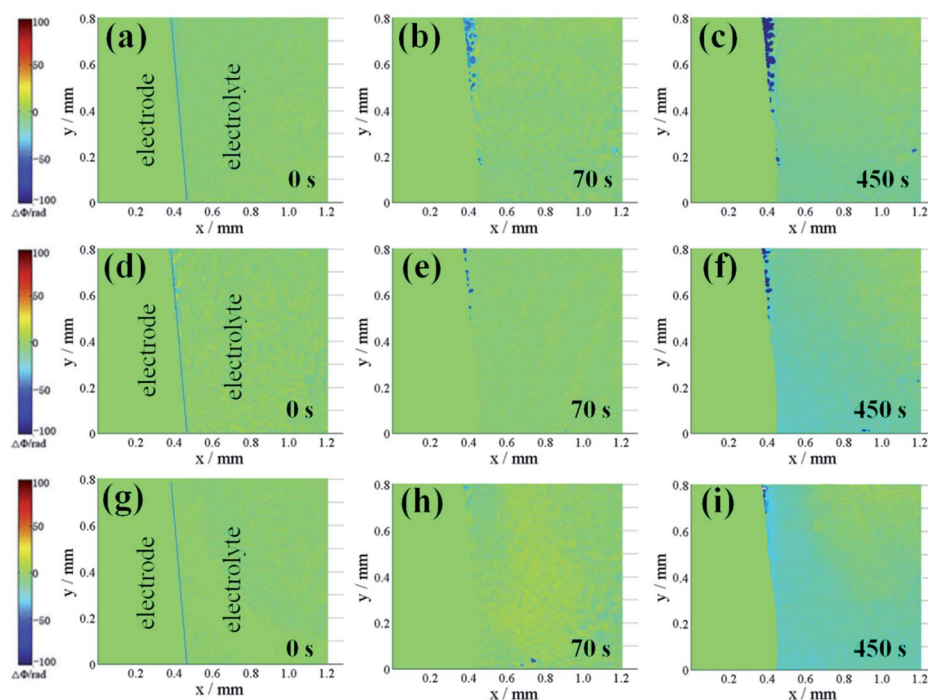


Fig. 6 The corresponding distributions of the optical difference at various times relative to the initial time and corresponding to different CV potentials, (a–c) HTTFs-1h, (d–f) TiO_2 , and (g–i) TiN.

high rate capability and cycle stability of the HTTF anode, the CV of HTTFs-1h and pure TiO₂ at various scan rate ranges from 0.2 to 2.0 mV s⁻¹ was measured to investigate the electrochemical kinetics toward Na⁺. As seen in Fig. 5a and b, the shapes of the CV curves for HTTFs-1h and pure TiO₂ at different scan rates are similar. With the increase of sweep rate, the shifts of the cathodic/anodic peaks for HTTFs-1h (Fig. 5a) were much smaller than those of pure TiO₂ (Fig. 5b), indicating that the diffusion of sodium ions has been greatly improved. According to the relationship between the peak current density (*i*) and scan rate (*v*),^{25,47}

$$i = av^b \quad (1)$$

or

$$\log i = \log a + b \log v \quad (2)$$

As is well known, the *b*-value is the ratio of capacitance contribution, ranging from 0.5 to 1.0. In detail, *b* = 1 means that sodium ion storage is completely controlled by the capacitive-controlled process, while *b* = 0.5 means that the process is absolutely dominated by the diffusion-controlled process. The *b* value of HTTFs-1h is 0.98335, which is higher than that of pure TiO₂ (0.89166), indicating higher capacitance contribution for HTTFs-1h (Fig. 5c). In addition, capacitive-controlled behavior was analyzed by the Dunn method. The capacitive and diffusion control charge in the total charge storage capacity at different rates can be analyzed based on eqn (3) or (4),⁴⁸

$$i(V) = k_1v + k_2v^{1/2} \quad (3)$$

or

$$i(V)/v^{1/2} = k_1v^{1/2} + k_2 \quad (4)$$

As presented in Fig. 5d, the capacitive contribution accounted for 82.13% of the total capacity on HTTFs-1h at 1 mV s⁻¹ (blue area). In comparison, the capacitance contribution ratio of pure TiO₂ is only 74.07% (Fig. 5e and f). It clearly indicated that capacitive behavior plays a dominant role in the storage mechanism of HTTFs-1h. It is worth mentioning that the capacitance contribution of HTTFs-1h becomes more obvious as the scan rate increased. The capacitance-controlled behavior of HTTFs-1h was mainly ascribed to the array nanosheets on the surface of the hollow fiber providing unrestricted channels for the insertion of sodium ions, and the self-built electric field brought by the interface effect accelerates the transmission of sodium ions. In addition, uniformly doped TiN causes more defect sites, and these defects are conducive to the ultra-high-speed storage of sodium ions. The results and our analysis can certify that the as-prepared HTTFs-1h material demonstrates outstanding rate capability and cycle stability performances.

Nondestructive, effective, and responsive *in situ* digital holography is employed to characterize the acceleration of ions by self-built electric fields during electrochemical reactions.⁴⁹

The electrochemical performance of the cells tested in a transparent mold (Fig. S11a†) is first presented in Fig. S11b.† According to the relationship between the phase difference ($\Delta\Phi$), the solution refractive index (Δn), and the solution concentration (ΔC) are presented as follows:

$$\Delta C = k \times \Delta n = (k \cdot \lambda_0 / 2\pi d) \Delta\Phi \quad (5)$$

k means the concentrative refractivity; λ_0 represents the wavelength of the laser light; *d* is the geometrical path length where a refractive index variation exists. In each phase map, the right part corresponds to the electrolyte, and the left part represents the electrode. Any change in the dissolved species can lead to a shift in the phase difference ($\Delta\Phi$) at the interface, where $\Delta\Phi < 0$ signifies a decrease in concentration, and $\Delta\Phi > 0$ equates to an increase. Such a shift is observed as a color change in Fig. 6a–i, as a result of the ongoing electrochemical reaction. Compared with TiO₂ (Fig. 6d–f) and TiN (Fig. 6g–i), when sodium ions are intercalated into HTTFs-1h (Fig. 6a–c) at the same time, the reduction of sodium ions at the interface is higher, and the ion concentration decreases obviously at the peak in the CV curve (Fig. S11b†). This proves that the self-built electric field of the heterogeneous structure can accelerate ion diffusion and electron transfer during charging and discharging.

Conclusions

In summary, we have developed a simple structure-induced partial phase transition strategy to modify anatase TiO₂ for Na ion batteries. By adjusting the ammonia annealing time (0.5, 1, and 2 h), multi-level HTTFs with different component contents were successfully prepared which exerted the interface effect on the acceleration of charge transfer. HTTFs-1h demonstrates excellent rate capability and long-term cycling performance. HTTFs-1h delivered reversible capacity as high as 270.9 mA h g⁻¹ at 50 mA g⁻¹, and the capacity maintained at 113.1 mA h g⁻¹ at a superhigh current density of 10 000 mA g⁻¹. Additionally, the HTTFs-1h electrode still maintains a capacity of 132.5 mA h g⁻¹ after 10 000 cycles at an extremely high current density of 5000 mA g⁻¹, and the coulombic efficiency is almost 100%. Experimental results and DFT calculations reveal the superior electrochemical performance of HTTFs-1h. This can be attributed to the fact that the hollow nanofibers composed of array-like nanosheets provide a shorter charge transfer channel and the highly conductive TiN doping improves the intrinsic conductivity of TiO₂. The introduced interface effect significantly increases the rate of sodium ion transfer. These improvements demonstrate that the structure-induced partial phase transition to construct a heterogeneous interface is an effective strategy to improve the electrochemical performance of advanced battery materials.

Author contributions

Guo Hong and Yagang Yao conceived and designed the research. Pan Xue and Qiulong Li participated in the material and electrode preparation, cell fabrication, and device test or

interpretation of results. Weigao Xu, Jingyu Sun and Zhongfan Liu participated in the result discussion and data analysis. Pan Xue wrote the paper. Wenbin Gong and Zhongti Sun conducted theoretical calculations. Han Wang, Kaiping Zhu and Can Guo participated in the collection and correction of article data. Weigao Xu and Yagang Yao supervised the project.

Conflicts of interest

There are no conflicts to declare.

Acknowledgements

This work was supported by the Fundamental Research Funds for the Central Universities (grant number: 14380231); The National Natural Science Foundation of China (grant number 21873048); The Natural Science Foundation of Jiangsu Province (grant number BK20180319); Guo Hong acknowledges the research fund of University of Macau, Macau SAR (File no. MYRG2018-00079-IAPME, MYRG2019-00115-IAPME), and the Science and Technology Development Fund, Macau SAR (0059/2018/A2, 009/2017/AMJ).

References

- 1 T. W. Chen, P. Zhao, X. Guo and S. L. Zhang, *Nano Lett.*, 2017, **17**, 2299–2306.
- 2 G. W. Li, G. R. Blake and T. T. M. Palstra, *Chem. Soc. Rev.*, 2017, **46**, 1693–1706.
- 3 C. T. Zhao, C. Yu, B. Qiu, S. Zhou, M. D. Zhang, H. W. Huang, B. Q. Wang, J. J. Zhao, X. L. Sun and J. S. Qiu, *Adv. Mater.*, 2018, **30**, 1702486.
- 4 D. Kundu, E. Talaie, V. Duffort and L. F. Nazar, *Angew. Chem., Int. Ed.*, 2015, **54**, 3431–3448.
- 5 X. Chen, X. Shen, T.-Z. Hou, R. Zhang, H.-J. Peng and Q. Zhang, *Chem*, 2020, **6**, 1–15.
- 6 Y.-F. Zhu, Y. Xiao, W.-B. Hua, S. Indris, S.-X. Dou, Y.-G. Guo and S.-L. Chou, *Angew. Chem., Int. Ed.*, 2020, **59**, 9299–9304.
- 7 Y.-B. Niu, Y.-J. Guo, Y.-X. Yin, S.-Y. Zhang, T. Wang, P. Wang, S. Xin and Y.-G. Guo, *Adv. Mater.*, 2020, **32**, 2001419.
- 8 Z.-L. Xu, K. Lim, K.-Y. Park, G. Yoon, W. M. Seong and K. Kang, *Adv. Funct. Mater.*, 2018, **28**, 1802099.
- 9 B. Chen, Y. H. Meng, F. X. Xie, F. He, C. N. He, K. Davey, N. Q. Zhao and S.-Z. Qiao, *Adv. Mater.*, 2018, **30**, 1804116.
- 10 B. S. Li, B. J. Xi, Z. Y. Feng, Y. Lin, J. C. Liu, J. K. Feng, Y. T. Qian and S. J. Xiong, *Adv. Mater.*, 2018, **30**, 1705788.
- 11 H. Liu, W. Li, D. K. Shen, D. Y. Zhao and G. X. Wang, *J. Am. Chem. Soc.*, 2015, **137**, 13161–13166.
- 12 X. Y. Wang, L. Fan, D. C. Gong, J. Zhu, Q. F. Zhang and B. A. Lu, *Adv. Funct. Mater.*, 2016, **26**, 1104–1111.
- 13 H. N. He, D. Sun, Q. Zhang, F. Fu, Y. G. Tang, J. Guo, M. H. Shao and H. Y. Wang, *ACS Appl. Mater. Interfaces*, 2017, **9**, 6093–6103.
- 14 H. Usui, S. Yoshioka, K. Wasada, M. Shimizu and H. Sakaguchi, *ACS Appl. Mater. Interfaces*, 2015, **7**, 6567–6573.
- 15 Y. Z. Jiang, S. L. Yu, B. Q. Wang, Y. Li, W. P. Sun, Y. H. Lu, M. Yan, B. Song and S. X. Dou, *Adv. Funct. Mater.*, 2016, **26**, 5315–5321.
- 16 X. P. Hong, J. Kim, S.-F. Shi, Y. Zhang, C. H. Jin, Y. H. Sun, S. Tongay, J. Q. Wu, Y. F. Zhang and F. Wang, *Nat. Nanotechnol.*, 2014, **9**, 682–686.
- 17 Y. Zheng, T. Zhou, C. Zhang, J. Mao, H. Liu and Z. P. Guo, *Angew. Chem., Int. Ed.*, 2016, **55**, 3408–3413.
- 18 J. N. Hao, J. Zhang, G. L. Xia, Y. J. Liu, Y. Zheng, W. C. Zhang, Y. B. Tang, W. K. Pang and Z. P. Guo, *ACS Nano*, 2018, **12**, 10430–10438.
- 19 X. B. Liao, Y. L. Zhao, J. H. Wang, W. Yang, L. Xu, X. C. Tian, Y. Shuang, K. A. Owusu, M. Y. Yan and L. Q. Mai, *Nano Res.*, 2018, **11**, 2083–2092.
- 20 H. N. He, D. Huang, W. K. Pang, D. Sun, Q. Wang, Y. G. Tang, X. B. Ji, Z. P. Guo and H. Y. Wang, *Adv. Mater.*, 2018, **30**, 1801013.
- 21 H. C. Zhang, Y. Jiang, Z. Y. Qi, X. W. Zhong and Y. Yu, *Energy Storage Mater.*, 2018, **12**, 37–43.
- 22 K. S. Yang, Y. Dai and B. B. Huang, *J. Phys. Chem. C*, 2007, **111**, 18985–18994.
- 23 K. K. Ghuman and C. V. Singh, *J. Phys.: Condens. Matter*, 2013, **25**, 475501.
- 24 Y. Wu, Y. Jiang, J. N. Shi, L. Gu and Y. Yu, *Small*, 2017, **13**, 1700129.
- 25 L. Wang, G. R. Yang, J. N. Wang, S. L. Wang, C. Y. Wang, S. J. Peng, W. Yan and S. Ramakrishna, *Small*, 2019, **15**, 1901584.
- 26 M. Wang, Y. Yang, Z. Z. Yang, L. Gu, Q. W. Chen and Y. Yu, *Adv. Sci.*, 2017, **4**, 1600468.
- 27 H. A. Cha, H. M. Jeong and J. K. Kang, *J. Mater. Chem. A*, 2014, **2**, 5182–5186.
- 28 H. N. He, H. Y. Wang, D. Sun, M. H. Shao, X. B. Huang and Y. G. Tang, *Electrochim. Acta*, 2017, **236**, 43–52.
- 29 K. Gao, B. Wang, L. Tao, B. V. Cunning, Z. P. Zhang, S. Y. Wang, R. S. Ruoff and L. T. Qu, *Adv. Mater.*, 2019, **31**, 1805121.
- 30 B. F. Wang, F. Zhao, G. D. Du, S. Porter, Y. Liu, P. Zhang, Z. X. Cheng, H. K. Liu and Z. G. Huang, *ACS Appl. Mater. Interfaces*, 2016, **8**, 16009–16015.
- 31 Q. M. Gan, H. N. He, Y. H. Zhu, Z. Y. Wang, N. Qin, S. Gu, Z. Q. Li, W. Luo and Z. G. Lu, *ACS Nano*, 2019, **13**, 9247–9258.
- 32 T. H. Zhou, W. Lv, J. Li, G. M. Zhou, Y. Zhao, S. X. Fan, B. Liu, B. H. Li, F. Y. Kang and Q.-H. Yang, *Energy Environ. Sci.*, 2017, **10**, 1694–1703.
- 33 Q. L. Li, Q. C. Zhang, J. Sun, C. L. Liu, J. B. Guo, B. He, Z. Y. Zhou, P. Man, C. W. Li, L. Y. Xie and Y. G. Yao, *Adv. Sci.*, 2019, **6**, 1801379.
- 34 Q. L. Li, Q. C. Zhang, C. L. Liu, Z. Y. Zhou, C. W. Li, B. He, P. Man, X. N. Wang and Y. G. Yao, *J. Mater. Chem. A*, 2019, **7**, 12997–13006.
- 35 Y. Zheng, T. F. Zhou, X. D. Zhao, W. K. Pang, H. Gao, S. Li, Z. Zhou, H. K. Liu and Z. P. Guo, *Adv. Mater.*, 2017, **29**, 1700396.
- 36 Y. W. Liu, T. F. Zhou, Y. Zheng, Z. H. He, C. Xiao, W. K. Pang, W. Tong, Y. M. Zou, B. C. Pan, Z. P. Guo and Y. Xie, *ACS Nano*, 2017, **11**, 8519–8526.

- 37 L. B. Ma, X. Gao, W. J. Zhang, H. Yuan, Y. Hu, G. Y. Zhu, R. P. Chen, T. Chen, Z. X. Tie, J. Liu, T. Wu and Z. Jin, *Nano Energy*, 2018, **53**, 91–96.
- 38 C. J. Chen, Y. W. Wen, X. L. Hu, X. L. Ji, M. Y. Yan, L. Q. Mai, P. Hu, B. Shan and Y. H. Huang, *Nat. Commun.*, 2015, **6**, 6929–6936.
- 39 V. Etacheri, J. E. Yourey and B. M. Bartlett, *ACS Nano*, 2014, **8**, 1491–1499.
- 40 T. Q. Lin, C. Y. Yang, Z. Wang, H. Yin, X. J. Lu, F. Q. Huang, J. H. Lin, X. M. Xie and M. H. Jiang, *Energy Environ. Sci.*, 2014, **7**, 967–972.
- 41 F. Zuo, K. Bozhilov, R. J. Dillon, L. Wang, P. Smith, X. Zhao, C. Bardeen and P. Y. Feng, *Angew. Chem., Int. Ed.*, 2012, **51**, 6223–6226.
- 42 L. M. Wu, D. Bresser, D. Buchholz, G. A. Giffin, C. R. Castro, A. Ochel and S. Passerini, *Adv. Energy Mater.*, 2015, **5**, 1401142.
- 43 G. Q. Zou, J. Chen, Y. Zhang, C. Wang, Z. D. Huang, S. M. Li, H. X. Liao, J. F. Wang and X. B. Ji, *J. Power Sources*, 2016, **325**, 25–34.
- 44 Y. Zhang, C. W. Foster, C. E. Banks, L. D. Shao, H. S. Hou, G. Q. Zou, J. Chen, Z. D. Huang and X. B. Ji, *Adv. Mater.*, 2016, **28**, 9391–9399.
- 45 Y. Xiong, J. F. Qian, Y. L. Cao, X. P. Ai and H. X. Yang, *ACS Appl. Mater. Interfaces*, 2016, **8**, 16684–16689.
- 46 T. F. Zhou, Y. Zheng, H. Gao, S. D. Min, S. Li, H. K. Liu and Z. P. Guo, *Adv. Sci.*, 2015, **2**, 1500027.
- 47 Z. Chen, P. F. Zhao, Z. Y. Luo, M. B. Zheng, H. Tian, P. Gong, G. Gao, H. Pan, L. L. Liu, A. Q. Ma, H. D. Cui, Y. F. Ma and L. T. Cai, *ACS Nano*, 2016, **10**, 10049–10057.
- 48 G. Q. Zou, C. Wang, H. S. Hou, C. W. Wang, X. Q. Qiu and X. B. Ji, *Small*, 2017, **13**, 1700762.
- 49 C. Lai, B. Y. Yuan, H. L. Dai, K. Xi, C. J. Harris, C. Wang and R. V. Kumar, *J. Phys. Chem. C*, 2017, **121**, 24733.